

Predicting ionic conductivity in solids from the machine-learned potential energy landscape

Artem Maevskiy,^{1,*} Alexandra Carvalho,^{1,2} Emil Sataev,³ Volha Turchyna,³ Keian Noori,^{1,2} Aleksandr Rodin,^{4,5} A. H. Castro Neto,^{1,2,5,6} and Andrey Ustyuzhanin^{7,8,1}

¹*National University of Singapore, Institute for Functional Intelligent Materials, NUS S9 Building, 4 Science Drive 2, 117544 Singapore*

²*National University of Singapore, Centre for Advanced 2D Materials, 6 Science Drive 2, 117546 Singapore*

³*HSE University, Faculty of Computer Science, Pokrovsky Boulevard 11, 109028 Moscow, Russian Federation*

⁴*Yale-NUS College, 16 College Avenue West, 138527 Singapore*

⁵*National University of Singapore, Department of Materials Science Engineering, 9 Engineering Drive 1, 117575 Singapore*

⁶*National University of Singapore, Department of Physics, 2 Science Drive 3, 117551 Singapore*

⁷*Constructor Knowledge Labs, Bremen, Campus Ring 1, 28759, Germany*

⁸*Constructor University, Bremen, Campus Ring 1, 28759, Germany*

Discovering new superionic materials is essential for advancing solid-state batteries, which offer improved energy density and safety compared to the traditional lithium-ion batteries with liquid electrolytes. Conventional computational methods for identifying such materials are resource-intensive and not easily scalable. Recently, universal interatomic potential models have been developed using equivariant graph neural networks. These models are trained on extensive datasets of first-principles force and energy calculations. One can achieve significant computational advantages by leveraging them as the foundation for traditional methods of assessing the ionic conductivity, such as molecular dynamics or nudged elastic band techniques. However, the generalization error from model inference on diverse atomic structures arising in such calculations can compromise the reliability of the results. In this work, we propose an approach for the quick and reliable screening of ionic conductors through the analysis of a universal interatomic potential. Our method incorporates a set of heuristic structure descriptors that effectively employ the rich knowledge of the underlying model while requiring minimal generalization capabilities. Using our descriptors, we rank lithium-containing materials in the Materials Project database according to their expected ionic conductivity. Eight out of the ten highest-ranked materials are confirmed to be superionic at room temperature in first-principles calculations. Notably, our method achieves a speed-up factor of approximately 50 compared to molecular dynamics driven by a machine-learning potential, and is at least 3,000 times faster compared to first-principles molecular dynamics.

I. INTRODUCTION

Solid-state batteries (SSBs) are a promising alternative to traditional lithium-ion batteries due to their higher energy density and enhanced safety features. With the elimination of liquid electrolytes, SSBs reduce the risk of leakage and combustion, thus mitigating one of the major safety concerns with conventional batteries [1–3]. Coupled with the potential for increased energy storage [4], this safety enhancement makes SSBs a crucial technology for advancing electric vehicles and portable electronics, where the demand for longer battery life and robust performance is ever-increasing.

Despite these advantages, SSBs development faces a number of challenges that prevents their widespread adoption [5]. One major limitation is the relatively low ionic conductivity of solid electrolytes compared to their liquid counterparts, which can diminish the overall performance of the battery. Additionally, interface stability between the solid electrolyte and electrodes remains a critical issue [6, 7]. The formation of interfacial resistance and degradation over time can significantly impact the

lifespan and efficiency of a battery [6]. Therefore, there is a pressing need for the development of new solid-state electrolytes (SSEs) with improved properties to overcome these barriers.

To address these challenges, computational prediction methods have been employed to identify and optimize new SSE materials [8–12]. However, these methods are often computationally expensive and time-consuming. Machine learning (ML) presents a viable solution to mitigate these limitations [13–25]. By leveraging large datasets such as the Materials Project database [26] and advanced algorithms, ML has the potential to speed up the discovery of new materials with high ionic conductivity and therefore accelerate the research and development of high-performance SSBs [27, 28].

Different ML algorithms that have been employed to assist the discovery of superionic materials include classical supervised ML methods like logistic regression [29, 30], gradient boosting [31] and support vector machines [32, 33], classical unsupervised methods [27, 34], as well as deep learning approaches based on graph neural networks (GNN) [35–37] and transformers [38]. The main difficulty in implementing the ML models for identifying SSEs is in general the limited availability of high-quality data on ionic mobility in solids. This motivates the use of knowledge transfer methods [33], or trad-

* Contact author: maevskiy@nus.edu.sg

ing off for larger datasets [36] obtained using approximate methods [39].

The scarcity of available data drives the search for informative material descriptors that correlate well with ionic conductivity. This search is typically focused on descriptors that characterize compositions, geometric configurations, and electrochemical and electronic properties of materials [27, 40, 41], often relying on implementations from the `matminer` library [42], which are adapted from scientific publications. In this work, we aim to expand this focus by exploring the features of the interatomic potential (IAP).

While IAP can be evaluated with expensive first-principles density functional theory (DFT) calculations, ML models allow for bypassing this step. Since there is notably more high-quality data available for predicting interatomic forces and energies, the task of predicting IAP is far less constrained than identifying SSEs directly. In fact, various ML methods have been proposed in the past decades to effectively bypass DFT in IAP calculations [43–45].

A notable improvement in the performance and reliability of these methods has been observed after the adoption of graph neural networks (GNNs) [13–15]. These models inherently impose permutation invariance by operating on graph structures, where the order of nodes does not affect the computation of graph-level representations. Additionally, invariance under 3D translations and rotations is achieved through the use of equivariant message passing and invariant feature aggregation methods. Although most of the initial models utilize 2-body messages, the introduction of many-body messages and updates allowed models like CHGNet [17], M3GNet [16], MACE [18, 19, 21] and the NequIP-based [46] SevenNet [47] achieve significant quality improvement, as demonstrated on the Matbench Discovery public benchmark [48]. These models may also be called universal potentials, as they cover the majority of the elements in the periodic table that are highly relevant to applications.

In the context of ionic transport studies, ML-IAPs can serve as substitutes for DFT in MD [37] and nudged elastic band (NEB) calculations [49]. However, a notable concern with ML-IAPs is the generalization error, which refers to the error in the model’s predictions when applied to new data, unseen at training time. Naturally, one should expect this error to increase as MD and NEB simulations drive the studied systems further from the domain of the training set, leading to a decrease in the model’s predictive accuracy and reliability. A typical way of addressing this issue is through active learning [50, 51]. This involves controlling the prediction error, running DFT on configurations where the error is excessively large and then retraining the model on these configurations. While this approach effectively reduces the generalization error, it sacrifices some of the computational efficiency gained by switching from DFT to ML-IAPs.

In this work, we take a different approach by utilizing a universal potential model to design a set of dedicated descriptors that predict materials with high lithium mobility while minimizing generalization error. We leverage an ML-IAP trained on vast amounts of data to analyze the potential landscape in a controlled environment for the labeled structures present in high-quality computational and experimental Li conductivity datasets. From this analysis, we propose a set of heuristics that can be calculated on structure configurations that are similar to the examples used for training the potential. This ensures minimal generalization requirements for the model and therefore more accurate predictions of the interatomic potential in the diverse material environments. Finally, we use these descriptors to predict SSEs within the Materials Project database and validate our predictions with *ab initio* calculations.

The studies performed in this work are done using the M3GNet model, which was trained by the authors of the original work [16] on the entire Materials Project dataset [26]. It should be noted, however, that our approach is not specific to a particular model and could be used with any IAP.

This document is structured as follows: Sec. II describes the methodology used throughout this work, outlining the key ideas of the proposed approach in Secs. II A and II B, along with details of the *ab initio* calculations presented in Sec. II C. In Sec. III, we report and discuss our findings and provide an outlook. Finally, we conclude in Sec. IV.

II. METHODOLOGY

The overall computational pipeline performed in this work is shown in Fig. 1. We start from a machine-learned interatomic potential, which is used to analyze the potential energy surface (PES) for a given material. Then, a set of scalar heuristics is derived from the obtained PES. These descriptors are based on our intuition of which PES properties should correlate well with ionic mobility, and are inspired by the frozen host lattice idea behind the pinball model [52] and are similar to the pathway volume assessed with the bond-valence technique in [53]. We further validate our choice and evaluate the quality of the derived heuristics with labeled data, both simulated and experimental. Descriptors that demonstrate robustness and highest predictive power are chosen to rank the structures from the Materials Project dataset [26]. Finally, we perform computationally demanding *ab initio* molecular dynamics (AIMD) simulation to validate the candidates that are most promising according to our method. We describe our pipeline in greater detail throughout Secs. II A to II C.

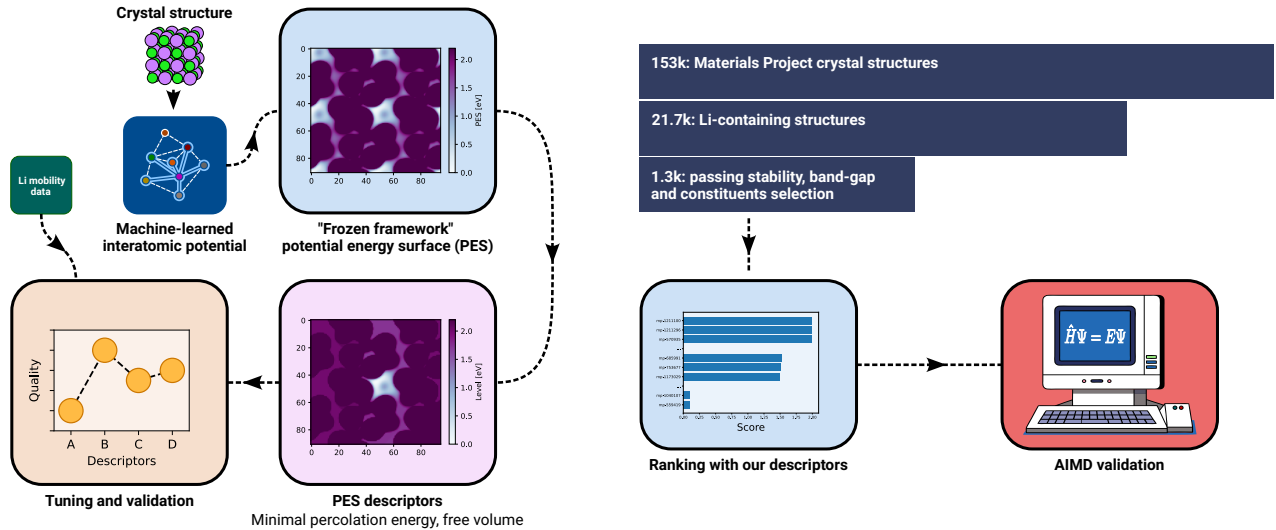


FIG. 1. Flowchart of the logical steps performed in our study

A. Potential energy surface in the frozen framework approximation

In this work, we leverage the assumption that the generalization error of the ML-IAP model is reduced when the system under study differs from the closest training object by only the coordinates of a single atom, compared to a system where all the atomic positions differ from those in the training set. Therefore, each structure is considered as having a single mobile ion per unit cell and a frozen framework formed by the remaining atoms. A potential energy surface (PES) scan is performed by placing the mobile ion at a set of locations on a regular 3d grid and evaluating the potential energy for the resulting structure. The grid spans over the entire unit cell with axes parallel to the lattice vectors. For each lattice vector \vec{l}_i , the grid step along that direction is $\vec{g}_i = \vec{l}_i/N_i$, where N_i is the smallest integer satisfying $|\vec{l}_i|/N_i \leq 0.25 \text{ \AA}$. Locations that are closer than $R_{\min} = 1.2 \text{ \AA}$ to any of the other atoms are excluded from this process to avoid ML-IAP evaluations on unphysical configurations.

Once the PES values on the grid are obtained, we repeat them along each axis to create a $2 \times 2 \times 2$ supercell. We position the origin of the grid so that the ion's lowest energy location is at the center of the supercell, with its 26 replicas located at the outer faces. In other words, the resulting PES is a 3-dimensional array with values corresponding to the mobile ion locations $\vec{r} = \sum_i (o_i + c_i) \cdot \vec{g}_i$, with $i \in \{1, 2, 3\}$, o_i being the grid coordinates for the minimal PES value and $c_i \in \{-N_i, \dots, N_i\}$. Then, a breadth-first search is performed for a minimum-energy-barrier path from the center to any of the faces of the supercell. *Minimal percolation energy* (MPE) for this ion is reported as the energy barrier value for the discovered path.

Due to the frozen framework approximation, MPE values are expected to be much larger than the actual activation energies. In reality, ionic hopping in superionic conductors occurs in a timescale of ns [54, 55], which allows for relaxation of the remaining ions and reduces the activation energies. However, our expectation is that MPE reflects the strength of the interactions that are overcome during ionic hopping, and thus correlates with the ionic mobility.

The breadth-first search of the optimal path requires calculating a quantity, which we denote as the *level map* (LM), given by:

$$\text{LM}(\vec{r}) \equiv \min_{C \in \mathcal{C}(\vec{r}, \vec{r}_0)} \left[\max_{\vec{r}' \in C} E(\vec{r}') \right], \quad (1)$$

where \vec{r}_0 is the initial location of the mobile atom at the relaxed state, $\mathcal{C}(\vec{r}, \vec{r}_0)$ is the set of all paths connecting \vec{r} and \vec{r}_0 , and $E(\vec{r}')$ is PES value at \vec{r}' . The meaning of LM is the minimal amount of energy an ion needs to be able to get to \vec{r} from its original site, within the frozen framework approximation. In our calculation, as explained above, the min and max operations are performed on a discrete grid. Using the level map concept, MPE can be defined as:

$$\text{MPE} \equiv \min_{\vec{r} \in \mathcal{F}} [\text{LM}(\vec{r})], \quad (2)$$

where \mathcal{F} denotes the set of points located at the faces of the supercell, where the replicas of the original site are located.

Finally, we introduce another family of structure characteristics that we call *free volumes* (FV) by calculating the average volume of PES/LM below a certain threshold

t:

$$FV_X(t) = \frac{1}{V} \int_{\text{supercell}} \mathbb{1} [X(\vec{r}) < t] d\vec{r}, \quad (3)$$

where V denotes the full volume of the supercell, $\mathbb{1}[\cdot]$ is the indicator function and $X(\vec{r})$ can be either $E(\vec{r})$ or $LM(\vec{r})$, in which case the corresponding FV is called *disconnected* or *connected*, respectively. This naming choice reflects that, by the definition of LM, any set of points satisfying $LM(\vec{r}) < T$ is a connected set, while this may not necessarily hold for $E(\vec{r})$.

Since a unit cell may contain more than one potentially mobile atom, aggregation is performed over atoms of the mobile species. For the case of MPE, the aggregation operation is just the minimum value of individual MPEs over the mobile atoms. For FVs, the aggregation is done by superimposing the indicator function outputs for different mobile atoms and combining them with logical OR operation prior to volume calculation.

In order to illustrate the way our method is intended to differentiate between good and bad ionic conductors, Fig. 2 shows the $LM(\vec{r}) = 0.5$ eV isosurfaces on top of two high-FV, one intermediate-FV and one low-FV structures. Within the frozen framework approximation, these isosurfaces highlight the regions accessible to the central Li atom of each structure under the given energy threshold. We expect the sizes of these regions, and hence their volumes, to correlate with Li mobility in a given material. While the threshold of 0.5 eV may seem extremely high, one should anticipate that the more accurate but expensive PES calculation with framework relaxation would have resulted in much lower LM values.

B. Validating PES descriptors

In order to evaluate our PES descriptors, we make use of two publicly available datasets related to lithium mobility and conductivity. The first dataset, KAHLE2020, from the study by L. Kahle et al. [10], includes high-throughput AIMD simulation of lithium diffusivity for 121 materials at 1000 K, with 25 of these materials also simulated at temperatures as low as 500 K. The second dataset, LASKOWSKI2023, is compiled by F. Laskowski et al. [27] in their study focused on identifying promising ionic conductors with a semi-supervised machine learning approach. The dataset consists of experimental conductivities from the literature, measured at or extrapolated to room temperature. It has 334 structures linked to the Inorganic Crystal Structure Database (ICSD) [57], 75 of which can also be successfully associated with entries from the Materials Project. To maximize the utility of the limited data, we ensure that our PES descriptors can highlight good ionic conductors in both the simulated and experimental datasets simultaneously. While our ultimate goal is to predict room-temperature superionic conductors, the prevalence of high-temperature labeled structures in the KAHLE2020 dataset is expected

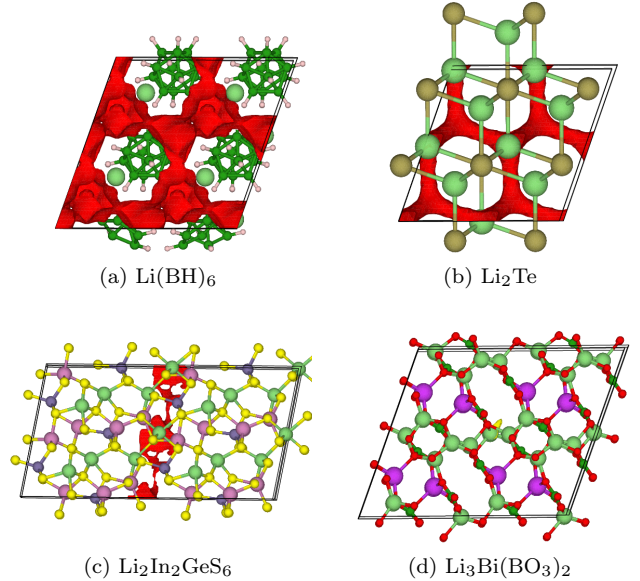


FIG. 2. *Level map isosurfaces at the threshold of 0.5 eV.* The corresponding structure compositions, Materials Project identifiers and values of the combined Ξ descriptor defined in Sec. II B (rounded to two digits) are: (a) $\text{Li}(\text{BH})_6 - \text{mp-1211296} - 0.99$, (b) $\text{Li}_2\text{Te} - \text{mp-2530} - 0.97$, (c) $\text{Li}_2\text{In}_2\text{GeS}_6 - \text{mp-1191476} - 0.35$, and (d) $\text{Li}_3\text{Bi}(\text{BO}_3)_2 - \text{mp-768738} - 0.00$. The isosurfaces are shown in red everywhere except (d), where yellow color is used for the isosurface and red is reserved to denote the oxygen atoms. The structures and isosurfaces are visualized using the VESTA software [56].

to improve our method's high-temperature predictions, which is still relevant for the mentioned ultimate goal.

The evaluation procedure is set up as follows. Firstly, since the KAHLE2020 dataset labels the structures with diffusion coefficients, we convert them to conductivity values via the Nernst-Einstein relation. We also extrapolate the conductivities to room temperature for those structures in KAHLE2020 where such extrapolation is possible. We then introduce two conductivity thresholds, σ^+ and σ^- , to label the structures with the conductivity above σ^+ (below σ^-) as good (bad) conductors. We smooth these labels with the assumption of Gaussian error distribution for the given conductivity values. That is, we weight the samples according to the value of the integral above σ^+ (below σ^-) for a Gaussian distribution with mean and standard deviation set to the given conductivity value and its uncertainty.

These labels and weights are then used to calculate ranking scores for each descriptor. Our scoring function is a modification of the commonly used area under the ROC-curve that only considers the lowest 10% of the false-positive rates instead of the full integral. This ensures that we aim towards maximal purity at the top of the list of structures and ignore the order in the lower portion of the list when using our descriptors for ranking potential ionic conductors. The resulting score values

for the MPE descriptor and FV descriptors at different energy thresholds are shown in Fig. 3.

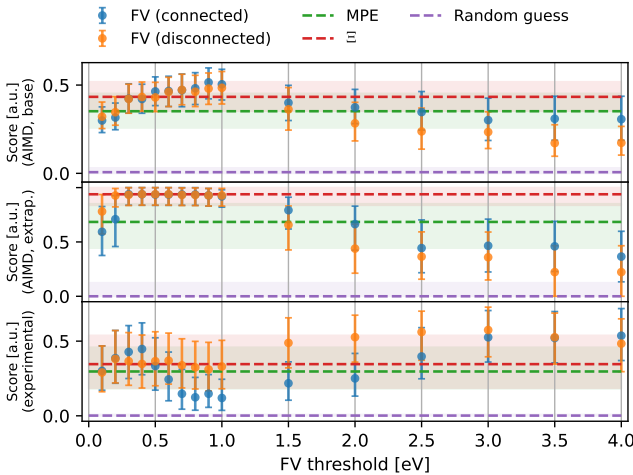


FIG. 3. *Descriptor evaluation scores.* The top panel shows the scores obtained with $T = 1000\text{ K}$ labels from the KAHLE2020 dataset. Scores obtained from that dataset with the alternative procedure, when positive classes are defined by the room-temperature-extrapolated conductivity values, are shown in the middle panel. The bottom panel contains the scores resulting from the experimentally measured conductivity labels reported at room temperature in the LASKOWSKI2023 dataset. The top-performing FV descriptors, based on all three evaluation scores, are combined into the SSE-ranking descriptor Ξ (see text) with its performance indicated by the dashed red line. For the reference, a random guess classifier performance is also shown (dashed purple line). The uncertainties are estimated with bootstrapping.

As most of the structures from the KAHLE2020 dataset are only simulated at $T = 1000\text{ K}$, we use the labels at that temperature throughout the dataset to obtain the scores shown in the top panel of Fig. 3, with thresholds set to $\sigma^+ = 0.1\text{ S/cm}$ and $\sigma^- = 0.01\text{ S/cm}$. In addition, we perform a separate evaluation, shown in the middle panel of Fig. 3, using the room-temperature-extrapolated conductivities when determining the positive classes with $\sigma^+ \approx 3.16\text{ mS/cm}$ (the exact relation being defined in log scale as $\log_{10}(\sigma^+[\text{S/cm}]) = -2.5$). For the LASKOWSKI2023 dataset, where all the experimental conductivity values are given at room temperature, we set the thresholds to $\sigma^+ = 0.05\text{ mS/cm}$ and $\sigma^- = 0.01\text{ mS/cm}$, resulting in the scores shown in the bottom panel of Fig. 3. As uncertainty values are not provided, we use an overestimate of 100% relative uncertainty in our weighting procedure. This, along with a lower conductivity threshold compared to that used in the simulated data analysis, is intended to smooth out the labels for intermediate-quality conductors.

One can see from Fig. 3 that all the proposed descriptors are capable of predicting ionic conductors to some degree, in the sense that they all have scores higher

than a random guess. It can also be noted that FV descriptors at thresholds of $0.3 - 0.5\text{ eV}$ demonstrate better or equal performance compared to MPE across all the three scores, while there is no particular winner between the connected and disconnected versions of FV. For that reason, we pick both versions of FV at the threshold of 0.5 eV to be further used for ranking the structures with unknown conductivities. We construct a combination of the two descriptors into the SSE-ranking descriptor, denoted as Ξ , by simultaneously thresholding them with a sigmoid function:

$$\Xi = S_1 \cdot S_2, \\ S_1 = s_{10} \left[2.00 + \log_{10} \text{FV}_{0.5\text{ eV}}^{\text{connected}} \right], \\ S_2 = s_{10} \left[1.15 + \log_{10} \text{FV}_{0.5\text{ eV}}^{\text{disconnected}} \right], \\ s_{10}(x) \equiv \frac{1}{1 + e^{-10x}}. \quad (4)$$

The threshold values of -2.00 and -1.15 for the base-10 logarithms of the connected and disconnected FV values, respectively, were picked to simultaneously discard the low-conductivity entries in both simulated and experimental data, as observed in Figs. 7 and 8 from Appendix B. The performance scores for the resulting Ξ descriptor is also shown in Fig. 3. Alternative ways of combining our descriptors for ranking are discussed in Appendix C.

The combined descriptor is then used to rank the Materials Project structures. We start by querying lithium containing structures with band gap of at least 0.5 eV and energy above hull of at most 0.05 eV/atom , which results in 5997 potential structures. By further discarding the entries containing transition metals we end up with 1302 structures, with 113 of them satisfying $\Xi > 0.25$, i.e. being above the two FV thresholds simultaneously. We then perform AIMD validation for the five of these structures with the largest Ξ values. Technical details for these simulations are given in Sec. II C, while the results are presented in Sec. III.

C. *Ab initio* molecular dynamics

Molecular dynamics simulations of selected structures with the highest Ξ values were carried out using the SIESTA code [58]. The forces were calculated using the generalized gradient approximation (GGA) of density functional theory [59], except for molecular solids, for which we used the LMKLL parameterization [60] of the van der Waals functional of Dion et al. [61]. The core electrons are represented by pseudopotentials of the Troullier-Martins scheme [62]. The basis sets for the Kohn-Sham states are linear combinations of numerical atomic orbitals, of the polarized double-zeta type [63, 64].

For each system, the volume relaxation was initially carried out for the primitive unit cell using a conjugate

gradient approach, and the Monkhorst and Pack Brillouin zone sampling grid [65] in the Materials Project data entry [26]. A supercell capable of accommodating a sphere with a diameter of at least 6.5 Å was then constructed and the self-consistent calculation of the charge density carried out using the Γ -point for Brillouin zone sampling. Then, a molecular dynamics calculation for the same system was carried out at constant temperature using a Nosé thermostat [66] and a maximum number of ten self-consistent iterations per time step. The integration time step of 1 fs was used. Additionally, a number of short cross-check AIMD runs with 0.25 and 0.5 fs step sizes were carried out and showed no significant impact on the observed results. The system is initially equilibrated in a NVT ensemble for 5 ps, after which we acquire data for the diffusivity calculation also in the NVT ensemble.

The diffusion coefficient is obtained by assuming three-dimensional Brownian motion with a mean square displacement (MSD) given by

$$\text{MSD} = \langle |\vec{r}(t) - \vec{r}(t_0)|^2 \rangle = 6D t_0, \quad (5)$$

where the ensemble average is over all ions. Since sampling trajectories for multiple starting configurations is prohibitive, we have instead split the trajectory into multiple time windows following the methodology used in [10]. We chose the window length of 15 ps and perform the linear fit on MSD from 1 to 15 ps in each window. The uncertainty for the diffusion coefficients is then estimated from the variance of these fit results over independent fits. A comparison of the diffusivity obtained using alternative fitting intervals can be found in Appendix D. The diffusion coefficients are converted to conductivity values using the Nernst-Einstein relation:

$$\sigma = \frac{nq^2}{k_B T} D, \quad (6)$$

where σ is the conductivity value, D is the extracted diffusion coefficient, k_B is the Boltzmann constant, T is the absolute temperature, n is the charge carrier concentration, and q is their charge.

We have also carried out tests for the finite system size effects for structure mp-1211296 which contains a comparatively small number of Li per supercell. To enable access to larger supercells and extended simulation times, we employed an ML-IAP (SevenNet) to drive the MD simulations in these tests. The results confirm that using larger supercells enhances the linearity of the MSD dependence. Notably, the diffusion coefficients extracted from the runs with different supercell sizes show consistent agreement within the statistical uncertainties.

III. RESULTS AND DISCUSSION

We have calculated MPE and FV descriptor values, as well as the SSE-ranking descriptor Ξ , for the 5997

structures from the Materials Project dataset that satisfy the minimal selection criteria, as discussed at the end of Sec. II B. These predictions are made public and can be found at [67]. We observe, that the top of the Ξ -ranked list is well populated by the structures from the LGPS family of superionic conductors [68], which supports the effectiveness of the proposed approach. For the optimal use of computational resources, we therefore focus our AIMD simulation on the other less-known structures from the top of the Ξ -ranked list. Additionally, a single well-known superionic conductor, $\text{Li}_7\text{P}_3\text{S}_{11}$ [69] is evaluated to validate our methodology. The summary of our findings is presented in Table I. AIMD validation results are also shown in Fig. 4, where the extracted conductivity values are plotted against $1/T$.

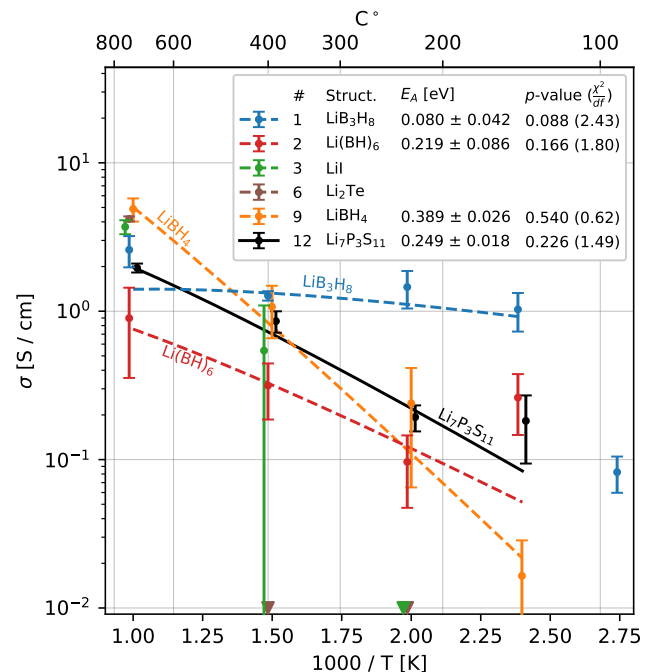


FIG. 4. AIMD conductivity values against $1/T$ for the top- Ξ structures. Vertical axis is clipped at minimal conductivity value of 10^{-2} S/cm with values below that threshold being indicated as triangles. While the target temperatures in our simulations are exactly 500, 667 and 1000 K (with the additional simulations at 417 and 363 K for some materials), small shifts are added to the horizontal axis values to improve marker visibility. The five LGPS-like structures from the top- Ξ list are omitted from our AIMD studies and therefore not shown in this plot.

A. AIMD validation summary

AIMD calculations for the reference $\text{Li}_7\text{P}_3\text{S}_{11}$ structure result in the activation barrier estimate of $E_A = 249 \pm 18 \text{ meV}$ and room-temperature-extrapolated conductivity of $7.9 \pm 3.7 \text{ mS/cm}$. These are consistent

#	MP identifier [26]	Composition	Ξ	AIMD results				
				T [K]	τ [ps]	σ [S / cm]	E_A [meV]	p -value ($\frac{\chi^2}{df}$)
1	mp-1211100	LiB_3H_8	0.9924	1000	53.7	2.6 ± 0.6	80 ± 42	0.09 (2.4)
				667	80.0	1.27 ± 0.09		
				500	104.8	1.5 ± 0.4		
				417	68.9	1.03 ± 0.30		
				363	97.4	$0.082 \pm 0.023^*$		
2	mp-1211296	$\text{Li}(\text{BH})_6$	0.9898	1000	60.8	0.9 ± 0.5	219 ± 86	0.17 (1.8)
				667	81.0	0.32 ± 0.13		
				500	70.3	0.10 ± 0.05		
				417	58.4	0.26 ± 0.12		
3	mp-570935	LiI	0.9812	1000	57.2	3.7 ± 0.4	-	-
				667	64.4	0.5 ± 0.6		
				500	66.2	$(2.2 \pm 1.0) \times 10^{-3}$		
4	mp-721239	$\text{Li}_{10}\text{Ge}(\text{PSe}_6)_2$	0.9746	-	-	-	-	-
5	mp-721252	$\text{Li}_{10}\text{Sn}(\text{PSe}_6)_2$	0.9729	-	-	-	-	-
6	mp-2530	Li_2Te	0.9712	1000	41.9	4.19 ± 0.17	-	-
				667	88.0	$(1.4 \pm 0.6) \times 10^{-3}$		
				500	47.9	$-(0.5 \pm 1.8) \times 10^{-3}$		
7	mp-721253	$\text{Li}_{10}\text{Si}(\text{PSe}_6)_2$	0.9712	-	-	-	-	-
8	mp-705516	$\text{Li}_{10}\text{Sn}(\text{PSe}_6)_2$	0.9661	-	-	-	-	-
9	mp-644223	LiBH_4	0.9647	1000	65.6	4.9 ± 0.9	389 ± 26	0.54 (0.6)
				667	92.9	1.1 ± 0.4		
				500	132.7	0.24 ± 0.17		
				417	92.8	0.016 ± 0.012		
10	mp-696127	$\text{Li}_{10}\text{Ge}(\text{PSe}_6)_2$	0.9645	-	-	-	-	-
12	mp-641703	$\text{Li}_7\text{P}_3\text{S}_{11}$	0.9606	1000	69.5	1.96 ± 0.14	249 ± 18	0.23 (1.5)
				667	85.6	0.86 ± 0.14		
				500	119.7	0.193 ± 0.039		
				417	58.1	0.18 ± 0.09		
25	mp-696128	$\text{Li}_{10}\text{Ge}(\text{PS}_6)_2$	0.9379	-	-	-	-	-

TABLE I. *Top Ξ predictions and AIMD results summary.* Ten structures with highest Ξ values are shown. In addition, two known superionic conductors, $\text{Li}_7\text{P}_3\text{S}_{11}$ [69] and $\text{Li}_{10}\text{Ge}(\text{PS}_6)_2$ (LGPS) [70], are also provided for reference. AIMD simulation runs were conducted with five structures from the top-ten list that are not obtained from LGPS by element substitution [68], and also for one of the reference structures. T , τ and σ represent the temperature, simulated time, and extracted conductivity value, respectively, for each AIMD simulation run. E_A is the activation energy extracted by fitting the Arrhenius law for the diffusivity dependence on $1/T$ using weighted least squares, where applicable. To quantify the goodness of these fits, the χ^2 -statistic divided by the number of degrees of freedom ($\frac{\chi^2}{df}$) is reported along with the corresponding p -value. The conductivity measurement marked by the * symbol was excluded from the Arrhenius law fit (see Fig. 4).

with the range of values measured experimentally, with $E_A = 295$ meV and $\sigma = 8.3$ mS / cm for the most pure phase sample in Ref. [71] and the lowest activation energy of $E_A = 124$ meV, with $\sigma = 3.2$ mS / cm in Ref. [72].

At the top of the list, we find three hydroborate structures, LiB_3H_8 (mp-1211100), $\text{Li}(\text{BH})_6$ (mp-1211296) and LiBH_4 (mp-644223). These belong to the family of lithium hydroborates, of which the best studied is hexagonal LiBH_4 [73–75]. The latter has been found experimentally to have an ionic conductivity of the order of 1 mS / cm at 383 K. Cubic $\text{Li}(\text{BH})_6$ has been found to have low diffusivity by a combined DFT and ML-

IAP study, but a closely connected orthorhombic distortion of the structure was found to have a conductivity of up to 0.1 S / cm at 700 K [76]. In our AIMD calculations, all the three hydroborates show significant ionic mobility in the studied temperature range. For LiBH_4 , the room-temperature-extrapolated conductivity is 0.44 ± 0.30 mS / cm. The other two hydroborates deviate from Arrhenius behavior at lower temperatures, preventing reliable extrapolation of their conductivity values to room temperature. Exclusively for LiB_3H_8 , which shows very high conductivity and lowest activation energy in the temperature range 417 – 1000 K, we perform

additional AIMD simulation at $T = 363\text{ K}$ yielding a conductivity value of $82 \pm 23\text{ mS/cm}$. This additional measurement is not included in the Arrhenius law fit reported in Table I and Fig. 4. Including this point yields $E_A = 216 \pm 31\text{ meV}$ with a very low p -value ($\frac{\chi^2}{df}$) of 0.003 (4.7). Since these hydroborates are molecular solids, the anions have rotational degrees of freedom, and these have been shown to be necessary for the high cationic conductivity in $\text{Li}(\text{BH})_6$ [77, 78]. Anionic motion is also apparent on the MSD of the non-Li ions (framework) in the AIMD calculations for $\text{Li}(\text{BH})_6$ and LiBH_4 .

LiI (mp-570935) also exhibits high mobility at 1000 K, but accompanied by observable diffusivity of the framework ions, which may indicate that 1000 K is close to the melting point. At $T = 500\text{ K}$, no diffusivity is observed. Interestingly, in the 667 K run, we see an abrupt change in lithium conductivity from zero during the first 35 ps of the simulation to over 1 S / cm in the subsequent 30 ps, indicating a transition to a highly diffusive state. The value of $0.5 \pm 0.6\text{ S/cm}$, shown in Table I and Fig. 4, is obtained by applying our MSD analysis procedure described in Sec. II C to the entire run, which includes both low- and high-diffusivity segments. Experimentally, wurtzite LiI is metastable and has been observed [79] but is very hygroscopic and hard to work with. Most ionic conductivity studies employing LiI use cubic LiI as a minor fraction of the electrolyte mixture [80].

Finally, Li_2Te (mp-2530) showed high diffusivity only at $T = 1000\text{ K}$, while no diffusion could be observed at lower temperatures over the affordable simulation times.

Of the five LGPS-like structures from Table I, $\text{Li}_{10}\text{Ge}(\text{PSe}_6)_2$ (mp-721239) was simulated in [68], and the reported activation energy and conductivity at room temperature are $190 \pm 40\text{ meV}$ and 24 mS/cm , respectively. The other structure of the same composition, mp-696127, is a slightly less stable concrete realization of the same anion-substituted disordered LGPS-like structure, and the two are expected to be mixed at room temperature. The remaining single $\text{Li}_{10}\text{Si}(\text{PSe}_6)_2$ and the two concrete realizations of $\text{Li}_{10}\text{Sn}(\text{PSe}_6)_2$ were not directly studied via AIMD in [68], while individual substitutions of $\text{Ge} \rightarrow \text{Sn/Si}$ and $\text{S} \rightarrow \text{Se}$ were all shown to produce superionic materials. Assuming that this also holds for the combined substitutions, we can confirm eight of the ten top- Ξ structures to be superionic.

B. ML-driven MD validation summary

Additionally, we perform a larger-scale validation of our results using an ML-IAP as the backbone for the MD. For this study exclusively, we employ the SevenNet model [47]. It has ~ 4 times more parameters and is trained on ~ 10 times more data than M3GNet, which is used throughout this work, and generally outperforms it on the Matbench Discovery benchmark. The technical details for this SevenNet-driven validation procedure can be found in Appendix A.

We find that 55% of the top-100 Ξ -ordered list of structures exhibit room temperature conductivity above 0.1 mS/cm , while that proportion for an unbiased sample is only $\sim 7\%$ (2 out of 29), as predicted by SevenNet-driven MD. Hence, we observe an approximately 8-fold increase in the number of positive examples through our selection method. At the same time, SevenNet-driven MD predicts room temperature conductivity below 0.005 mS/cm for 39% of the Ξ -selected structures. This discrepancy in predictions between our Ξ -based selection and SevenNet MD indicates that there likely are mechanisms not captured by the FV descriptors that inhibit high ionic conductivity. It may also be attributed to the limitations of the frozen framework approximation and potential errors in the M3GNet and SevenNet predictions.

C. Discussion

Both ML-driven MD and AIMD validation procedures confirm the significant enhancement of the amount of room-temperature superionic materials in the sample selected using the descriptors proposed in this work. Our method achieves even higher-purity samples if we only consider the diffusivity at 1000 K MD simulations: all of the AIMD-tested structures are diffusive at that temperature, and 88% out of top-100 are diffusive in the ML-driven MD validation. This may be due to the fact that most of the positive labels our method was tuned on are found in the KAHLE2020 dataset, which consists of primarily $T = 1000\text{ K}$ AIMD diffusion data. In this case, we can expect even higher performance from the proposed method once more high-quality room-temperature conductivity data becomes available.

The highest- Ξ structure we found, LiB_3H_8 (mp-1211100), demonstrates exceptional Li conductivity in our AIMD studies. The SevenNet-driven MD also ranks this material with highest extrapolated room temperature conductivity, which is an order of magnitude higher compared with the same estimate for the reference $\text{Li}_7\text{P}_3\text{S}_{11}$ material. To the best of our knowledge, this material has not been studied experimentally as a potential SSB electrolyte before, although the similar NaB_3H_8 structure has previously been successfully used in a composite solid electrolyte in a sodium-metal SSB [81, 82]. Ionic conductivity and relaxation times for anionic reorientation have also been studied for various phases of the related KB_3H_8 [83, 84].

The prevalence of the hydroborate structures family at the top of the Ξ -ordered list, which are known to be good ionic conductors, demonstrates the remarkable generalization capability of the proposed method. Notably, there are no examples of positively labeled hydroborate electrolytes in either of the datasets that we used for tuning.

We acknowledge that our descriptors cannot capture the full complexity of the dynamical effects that define

the ionic conductivity in solids [85–87]. However, the effectiveness observed in our screening suggests potential correlations between the complex dynamics of ionic motion and the characteristics derived from the simplified static picture that we utilize.

Finally, we note that our proposed descriptors are also relatively fast to calculate compared to other methods for predicting superionic materials, including ML-driven MD. Performing the entire PES analysis on the 5997 structures from the Materials Project database took us seven days on a single machine with 48-core Intel Xeon w7-3455 CPU and two 46-GB NVIDIA RTX 6000 Ada Generation GPUs. For comparison, it took us approximately same time to run ML-driven MD for only 100 materials on the same hardware.

D. Outlook

The findings presented in this study pave the way for further exploration in the field of ionic conductors for SSBs. Firstly, while our search focused on structures within the Materials Project database, extending this analysis to other databases, such as ICSD [57] and Alexandria [88, 89], is straightforward and may reveal additional promising materials.

Secondly, while the SSE-ranking descriptor Ξ was derived by manually combining the two best-performing descriptors, applying multivariate analysis and ML techniques to the entire set of descriptors could extract even more information from the available data and enhance prediction performance. Moreover, we anticipate that even greater improvements will become evident as more high-quality room-temperature conductivity data becomes available.

Another important direction is the extension of our approach to sodium conductors. We believe that the methodology outlined in our work can be readily applied to identify promising Na-based superionic materials. This could facilitate the advancement of sodium-ion SSBs, which are attracting interest due to their potential for lower costs and abundant raw materials [90].

Finally, the pipeline we have developed is well-suited for generative modeling applications [91, 92]. Both MPE and FV descriptors could be implemented in a differentiable manner, enabling the calculation of gradients with respect to atomic positions and element type embeddings

in the underlying machine learning interatomic potential models. These gradients could be utilized in a generative framework to guide the discovery of novel materials with high ionic conductivity.

IV. CONCLUSION

Our study presents an effective method for the rapid screening of solid electrolyte candidates using heuristic descriptors derived from interatomic potentials. By applying our proposed pipeline, supported by a universal machine-learned interatomic potential, we screened 1302 compounds from the Materials Project database, identifying several promising SSE candidates. AIMD simulations of the 10 highest-ranking materials confirm that all are conductive at high temperatures, with 8 out of 10 being superionic at room temperature. Notably, our approach highlights the solid electrolyte LiB_3H_8 ([mp-1211100](#)), with an impressive AIMD ionic conductivity estimate of $82 \pm 23 \text{ mS/cm}$ at $T = 363 \text{ K}$. To our knowledge, this material has not been studied experimentally in the context of SSBs.

V. DATA AVAILABILITY STATEMENT

The code implementing the proposed technique, as well as the predictions calculated for lithium-containing structures from the Materials Project, are available in [67].

VI. ACKNOWLEDGEMENTS

This research project is supported by the Ministry of Education, Singapore, under its Research Centre of Excellence award to the Institute for Functional Intelligent Materials, National University of Singapore (I-FIM, project No. EDUNC-33-18-279-V12). This research/project is supported by the National Research Foundation, Singapore under its AI Singapore Programme (AISG Award No: AISG3-RP-2022-028). This work used computational resources of the Singapore National Supercomputing Centre (NSCC) of Singapore. For the exploratory phase, this work used computational resources of the Constructor Research Platform provided by Constructor Technologies.

[1] J. G. Kim, B. Son, S. Mukherjee, N. Schuppert, A. Bates, O. Kwon, M. J. Choi, H. Y. Chung, and S. Park, A review of lithium and non-lithium based solid state batteries, *J. Power Sources* **282**, 299 (2015).

[2] C. Li, Z. Wang, Z. He, Y. Li, J. Mao, K. Dai, C. Yan, and J. Zheng, An advance review of solid-state battery: challenges, progress and prospects, *SM&T* **29**, e00297 (2021).

[3] J. Janek and W. G. Zeier, Challenges in speeding up solid-state battery development, *Nat. Energy.* **8**, 230 (2023).

[4] N. J. Dudney, W. C. West, and J. Nanda, *Handbook of solid state batteries*, 2nd ed., Vol. 6 (World Scientific, Singapore, 2015).

[5] Q. Zhao, S. Stalin, C.-Z. Zhao, and L. A. Archer, Designing solid-state electrolytes for safe, energy-dense batter-

ies, *Nature Reviews Materials* **5**, 229 (2020).

[6] C. Chen, M. Jiang, T. Zhou, L. Raijmakers, E. Vezhlev, B. Wu, T. U. Schülli, D. L. Danilov, Y. Wei, R.-A. Eichel, *et al.*, Interface aspects in all-solid-state Li-based batteries reviewed, *Advanced energy materials* **11**, 2003939 (2021).

[7] N. Ohta, K. Takada, L. Zhang, R. Ma, M. Osada, and T. Sasaki, Enhancement of the high-rate capability of solid-state lithium batteries by nanoscale interfacial modification, *Advanced Materials* **18**, 2226 (2006).

[8] A. Rodin, K. Noori, A. Carvalho, and A. H. Castro Neto, Microscopic theory of ionic motion in solids, *Phys. Rev. B* **105**, 224310 (2022).

[9] A. Carvalho, S. Negi, and A. H. C. Neto, Direct calculation of the ionic mobility in superionic conductors, *Scientific Reports* **12**, 19930 (2022).

[10] L. Kahle, A. Marcolongo, and N. Marzari, High-throughput computational screening for solid-state li-ion conductors, *Energy Environ. Sci.* **13**, 928 (2020).

[11] S. Muy, J. Voss, R. Schlem, R. Koerver, S. J. Sedlmaier, F. Maglia, P. Lamp, W. G. Zeier, and Y. Shao-Horn, High-throughput screening of solid-state Li-ion conductors using lattice-dynamics descriptors, *iScience* **16**, 270 (2019).

[12] Y. Wang, W. D. Richards, S. P. Ong, L. J. Miara, J. C. Kim, Y. Mo, and G. Ceder, Design principles for solid-state lithium superionic conductors, *Nature materials* **14**, 1026 (2015).

[13] K. Schütt, P.-J. Kindermans, H. E. Sauceda Felix, S. Chmiela, A. Tkatchenko, and K.-R. Müller, Schnet: A continuous-filter convolutional neural network for modeling quantum interactions, *Advances in neural information processing systems* **30** (2017).

[14] T. Xie and J. C. Grossman, Crystal graph convolutional neural networks for an accurate and interpretable prediction of material properties, *Physical review letters* **120**, 145301 (2018).

[15] C. Chen, W. Ye, Y. Zuo, C. Zheng, and S. P. Ong, Graph networks as a universal machine learning framework for molecules and crystals, *Chemistry of Materials* **31**, 3564 (2019).

[16] C. Chen and S. P. Ong, A universal graph deep learning interatomic potential for the periodic table, *Nature Computational Science* **2**, 718 (2022).

[17] B. Deng, P. Zhong, K. Jun, J. Riebesell, K. Han, C. J. Bartel, and G. Ceder, CHGNet as a pretrained universal neural network potential for charge-informed atomistic modelling, *Nature Machine Intelligence* **5**, 1031 (2023).

[18] I. Batatia, S. Batzner, D. P. Kovács, A. Musaelian, G. N. C. Simm, R. Drautz, C. Ortner, B. Kozinsky, and G. Csányi, The design space of $e(3)$ -equivariant atom-centered interatomic potentials, *arXiv:2205.06643* (2022).

[19] I. Batatia, D. P. Kovacs, G. N. C. Simm, C. Ortner, and G. Csanyi, MACE: Higher order equivariant message passing neural networks for fast and accurate force fields, in *Advances in Neural Information Processing Systems*, edited by A. H. Oh, A. Agarwal, D. Belgrave, and K. Cho (2022).

[20] A. Dunn, Q. Wang, A. Ganose, D. Dopp, and A. Jain, Benchmarking materials property prediction methods: the matbench test set and automatminer reference algorithm, *npj Computational Materials* **6**, 138 (2020).

[21] I. Batatia, P. Benner, Y. Chiang, A. M. Elena, D. P. Kovács, J. Riebesell, X. R. Advincula, M. Asta, W. J. Baldwin, N. Bernstein, *et al.*, A foundation model for atomistic materials chemistry, *arXiv:2401.00096* (2023).

[22] A. Merchant, S. Batzner, S. S. Schoenholz, M. Aykol, G. Cheon, and E. D. Cubuk, Scaling deep learning for materials discovery, *Nature* **624**, 80 (2023).

[23] C. Zeni, R. Pinsler, D. Zügner, A. Fowler, M. Horton, X. Fu, S. Shysheya, J. Crabbé, L. Sun, J. Smith, B. Nguyen, H. Schulz, S. Lewis, C.-W. Huang, Z. Lu, Y. Zhou, H. Yang, H. Hao, J. Li, R. Tomioka, and T. Xie, Mattergen: a generative model for inorganic materials design, *arXiv:2312.03687* (2024).

[24] H. Liu, S. Ma, J. Wu, Y. Wang, and X. Wang, Recent advances in screening lithium solid-state electrolytes through machine learning, *Frontiers in Energy Research* **9**, 639741 (2021).

[25] Q. Hu, K. Chen, F. Liu, M. Zhao, F. Liang, and D. Xue, Smart materials prediction: Applying machine learning to lithium solid-state electrolyte, *Materials* **15**, 1157 (2022).

[26] A. Jain, S. P. Ong, G. Hautier, W. Chen, W. D. Richards, S. Dacek, S. Cholia, D. Gunter, D. Skinner, G. Ceder, and K. A. Persson, Commentary: The materials project: A materials genome approach to accelerating materials innovation, *APL materials* **1**, 011002 (2013).

[27] F. A. Laskowski, D. B. McHaffie, and K. A. See, Identification of potential solid-state li-ion conductors with semi-supervised learning, *Energy & Environmental Science* **16**, 1264 (2023).

[28] A. D. Sendek, G. Cheon, M. Pasta, and E. J. Reed, Quantifying the search for solid li-ion electrolyte materials by anion: a data-driven perspective, *The Journal of Physical Chemistry C* **124**, 8067 (2020).

[29] A. D. Sendek, Q. Yang, E. D. Cubuk, K.-A. N. Duerloo, Y. Cui, and E. J. Reed, Holistic computational structure screening of more than 12000 candidates for solid lithium-ion conductor materials, *Energy & Environmental Science* **10**, 306 (2017).

[30] A. D. Sendek, E. D. Cubuk, E. R. Antoniuk, G. Cheon, Y. Cui, and E. J. Reed, Machine learning-assisted discovery of solid Li-ion conducting materials, *Chemistry of Materials* **31**, 342 (2019).

[31] E. Choi, J. Jo, W. Kim, and K. Min, Searching for mechanically superior solid-state electrolytes in li-ion batteries via data-driven approaches, *ACS applied materials & interfaces* **13**, 42590 (2021).

[32] K. Fujimura, A. Seko, Y. Koyama, A. Kuwabara, I. Kishida, K. Shitara, C. A. Fisher, H. Moriwake, and I. Tanaka, Accelerated materials design of lithium superionic conductors based on first-principles calculations and machine learning algorithms, *Advanced Energy Materials* **3**, 980 (2013).

[33] E. D. Cubuk, A. D. Sendek, and E. J. Reed, Screening billions of candidates for solid lithium-ion conductors: A transfer learning approach for small data, *The Journal of chemical physics* **150** (2019).

[34] Y. Zhang, X. He, Z. Chen, Q. Bai, A. M. Nolan, C. A. Roberts, D. Banerjee, T. Matsunaga, Y. Mo, and C. Ling, Unsupervised discovery of solid-state lithium ion conductors, *Nature communications* **10**, 5260 (2019).

[35] Z. Ahmad, T. Xie, C. Maheshwari, J. C. Grossman, and V. Viswanathan, Machine learning enabled computational screening of inorganic solid electrolytes for sup-

pression of dendrite formation in lithium metal anodes, *ACS central science* **4**, 996 (2018).

[36] Z. Wang, Y. Han, J. Cai, A. Chen, and J. Li, An end-to-end artificial intelligence platform enables real-time assessment of superionic conductors, *SmartMat* **4**, e1183 (2023).

[37] X. Guo, Z. Wang, J.-H. Yang, and X.-G. Gong, Machine-learning assisted high-throughput discovery of solid-state electrolytes for li-ion batteries, *Journal of Materials Chemistry A* **12**, 10124 (2024).

[38] C. J. Hargreaves, M. W. Gaulois, L. M. Daniels, E. J. Watts, V. A. Kurlin, M. Moran, Y. Dang, R. Morris, A. Morscher, K. Thompson, M. A. Wright, B.-E. Prasad, F. Blanc, C. M. Collins, C. A. Crawford, B. B. Duff, J. Evans, J. Gamon, G. Han, B. T. Leube, H. Niu, A. J. Perez, A. Robinson, O. Rogan, P. M. Sharp, E. Shoko, M. Sonni, W. J. Thomas, A. Vasylenko, L. Wang, M. J. Rosseinsky, and M. S. Dyer, A database of experimentally measured lithium solid electrolyte conductivities evaluated with machine learning, *npj Computational Materials* **9**, 9 (2023).

[39] Y. Nishitani, S. Adams, K. Ichikawa, and T. Tsujita, Evaluation of magnesium ion migration in inorganic oxides by the bond valence site energy method, *Solid State Ionics* **315**, 111 (2018).

[40] S.-H. Jang, Y. Tateyama, and R. Jalem, High-Throughput Data-Driven Prediction of Stable High-Performance Na-Ion Sulfide Solid Electrolytes, *Advanced Functional Materials* **32**, 2206036 (2022).

[41] B. He, S. Chi, A. Ye, P. Mi, L. Zhang, B. Pu, Z. Zou, Y. Ran, Q. Zhao, D. Wang, *et al.*, High-throughput screening platform for solid electrolytes combining hierarchical ion-transport prediction algorithms, *Scientific Data* **7**, 151 (2020).

[42] L. Ward, A. Dunn, A. Faghaninia, N. E. Zimmermann, S. Bajaj, Q. Wang, J. Montoya, J. Chen, K. Bystrom, M. Dylla, K. Chard, M. Asta, K. A. Persson, G. J. Snyder, I. Foster, and A. Jain, Matminer: An open source toolkit for materials data mining, *Computational Materials Science* **152**, 60 (2018).

[43] J. Behler and M. Parrinello, Generalized neural-network representation of high-dimensional potential-energy surfaces, *Physical review letters* **98**, 146401 (2007).

[44] A. P. Bartók, M. C. Payne, R. Kondor, and G. Csányi, Gaussian approximation potentials: The accuracy of quantum mechanics, without the electrons, *Physical review letters* **104**, 136403 (2010).

[45] A. P. Thompson, L. P. Swiler, C. R. Trott, S. M. Foiles, and G. J. Tucker, Spectral neighbor analysis method for automated generation of quantum-accurate interatomic potentials, *Journal of Computational Physics* **285**, 316 (2015).

[46] S. Batzner, A. Musaelian, L. Sun, M. Geiger, J. P. Mailoa, M. Kornbluth, N. Molinari, T. E. Smidt, and B. Kozinsky, E (3)-equivariant graph neural networks for data-efficient and accurate interatomic potentials, *Nature communications* **13**, 2453 (2022).

[47] Y. Park, J. Kim, S. Hwang, and S. Han, Scalable parallel algorithm for graph neural network interatomic potentials in molecular dynamics simulations, *Journal of Chemical Theory and Computation* **20**, 4857 (2024), pMID: 38813770.

[48] J. Riebesell, R. E. A. Goodall, P. Benner, Y. Chiang, B. Deng, A. A. Lee, A. Jain, and K. A. Persson, Mat-

bench Discovery – A framework to evaluate machine learning crystal stability predictions, arXiv:2308.14920 (2023).

[49] H. Jónsson, G. Mills, and K. W. Jacobsen, Nudged elastic band method for finding minimum energy paths of transitions, in *Classical and quantum dynamics in condensed phase simulations* (World Scientific, 1998) pp. 385–404.

[50] J. Zeng, D. Zhang, D. Lu, P. Mo, Z. Li, Y. Chen, M. Rynik, L. Huang, Z. Li, S. Shi, Y. Wang, H. Ye, P. Tuo, J. Yang, Y. Ding, Y. Li, D. Tisi, Q. Zeng, H. Bao, Y. Xia, J. Huang, K. Muraoka, Y. Wang, J. Chang, F. Yuan, S. L. Bore, C. Cai, Y. Lin, B. Wang, J. Xu, J.-X. Zhu, C. Luo, Y. Zhang, R. E. A. Goodall, W. Liang, A. K. Singh, S. Yao, J. Zhang, R. Wentzcovitch, J. Han, J. Liu, W. Jia, D. M. York, W. E. R. Car, L. Zhang, and H. Wang, DeePMD-kit v2: A software package for deep potential models, *J. Chem. Phys.* **159**, 054801 (2023).

[51] J. Qi, T. W. Ko, B. C. Wood, T. A. Pham, and S. P. Ong, Robust training of machine learning interatomic potentials with dimensionality reduction and stratified sampling, *npj Computational Materials* **10**, 43 (2024).

[52] L. Kahle, A. Marcolongo, and N. Marzari, Modeling lithium-ion solid-state electrolytes with a pinball model, *Phys. Rev. Mater.* **2**, 065405 (2018).

[53] S. Adams and J. Swenson, Determining ionic conductivity from structural models of fast ionic conductors, *Phys. Rev. Lett.* **84**, 4144 (2000).

[54] T. Morimoto, M. Nagai, Y. Minowa, M. Ashida, Y. Yokotani, Y. Okuyama, and Y. Kani, Microscopic ion migration in solid electrolytes revealed by terahertz time-domain spectroscopy, *Nature communications* **10**, 2662 (2019).

[55] E. van der Maas, T. Famprakis, S. Pieters, J. P. Dijkstra, Z. Li, S. R. Parnell, R. I. Smith, E. R. van Eck, S. Ganapathy, and M. Wagemaker, Re-investigating the structure–property relationship of the solid electrolytes $\text{Li}_{3-x} \text{In}_{1-x} \text{Zr}_x \text{Cl}_6$ and the impact of In–Zr (iv) substitution, *Journal of Materials Chemistry A* **11**, 4559 (2023).

[56] K. Momma and F. Izumi, *VESTA3* for three-dimensional visualization of crystal, volumetric and morphology data, *Journal of Applied Crystallography* **44**, 1272 (2011).

[57] D. Zagorac, H. Müller, S. Ruehl, J. Zagorac, and S. Rehme, Recent developments in the Inorganic Crystal Structure Database: theoretical crystal structure data and related features, *Journal of applied crystallography* **52**, 918 (2019).

[58] J. M. Soler, E. Artacho, J. D. Gale, A. García, J. Junquera, P. Ordejón, and D. Sánchez-Portal, The SIESTA method for ab initio order-N materials simulation, *J. Phys.: Condens. Matter* **14**, 2745 (2002).

[59] J. P. Perdew, K. Burke, and M. Ernzerhof, Generalized gradient approximation made simple, *Phys. Rev. Lett.* **77**, 3865 (1996).

[60] K. Lee, É. D. Murray, L. Kong, B. I. Lundqvist, and D. C. Langreth, Higher-accuracy van der Waals density functional, *Physical Review B* **82**, 081101 (2010).

[61] M. Dion, H. Rydberg, E. Schröder, D. C. Langreth, and B. I. Lundqvist, Van der Waals Density Functional for General Geometries, *Phys. Rev. Lett.* **92**, 246401 (2004).

[62] N. Troullier and J. L. Martins, Efficient pseudopotentials for plane-wave calculations, *Physical Review B* **43**, 1993 (1991).

[63] D. Sánchez-Portal, P. Ordejon, E. Artacho, and J. M. Soler, Density-functional method for very large systems with lcao basis sets, *International journal of quantum chemistry* **65**, 453 (1997).

[64] D. Sánchez-Portal, J. Junquera, Ó. Paz, and E. Artacho, Numerical atomic orbitals for linear-scaling calculations, *Phys. Rev. B* **64**, 235111 (2001).

[65] H. J. Monkhorst and J. D. Pack, Special points for brillouin-zone integrations, *Physical Review B* **13**, 5188 (1976).

[66] S. Nosé, A unified formulation of the constant temperature molecular dynamics methods, *J. Chem. Phys.* **81**, 511 (1984).

[67] (2024), https://constructor.app/platform/public/project/pes_fingerprint.

[68] S. P. Ong, Y. Mo, W. D. Richards, L. Miara, H. S. Lee, and G. Ceder, Phase stability, electrochemical stability and ionic conductivity of the $\text{Li}_{10\pm 1}\text{MP}_2\text{X}_{12}$ ($\text{M} = \text{Ge, Si, Sn, Al or P, and X = O, S or Se}$) family of superionic conductors, *Energy Environ. Sci.* **6**, 148 (2013).

[69] H. Yamane, M. Shibata, Y. Shimane, T. Junke, Y. Seino, S. Adams, K. Minami, A. Hayashi, and M. Tatsumisago, Crystal structure of a superionic conductor, $\text{Li}_7\text{P}_3\text{S}_{11}$, *Solid State Ionics* **178**, 1163 (2007).

[70] N. Kamaya, K. Homma, Y. Yamakawa, M. Hirayama, R. Kanno, M. Yonemura, T. Kamiyama, Y. Kato, S. Hama, K. Kawamoto, and A. Mitsui, A lithium superionic conductor, *Nature materials* **10**, 682 (2011).

[71] M. R. Busche, D. A. Weber, Y. Schneider, C. Dietrich, S. Wenzel, T. Leichtweiss, D. Schröder, W. Zhang, H. Weigand, D. Walter, S. J. Sedlmaier, D. Houtarde, L. F. Nazar, and J. Janek, In situ monitoring of fast Li-ion conductor $\text{Li}_7\text{P}_3\text{S}_{11}$ crystallization inside a hot-press setup, *Chemistry of Materials* **28**, 6152 (2016).

[72] F. Mizuno, A. Hayashi, K. Tadanaga, and M. Tatsumisago, High lithium ion conducting glass-ceramics in the system $\text{Li}_{2\text{S}}\text{--P}_2\text{S}_5$, *Solid State Ionics* **177**, 2721 (2006).

[73] M. Matsuo, Y. Nakamori, S.-i. Orimo, H. Maekawa, and H. Takamura, Lithium superionic conduction in lithium borohydride accompanied by structural transition, *Applied Physics Letters* **91**, 224103 (2007).

[74] L. Duchêne, A. Remhof, H. Hagemann, and C. Battaglia, Status and prospects of hydroborate electrolytes for all-solid-state batteries, *Energy Storage Materials* **25**, 782 (2020).

[75] H. Liu, X. Zhou, M. Ye, and J. Shen, Ion migration mechanism study of hydroborate/carborate electrolytes for all-solid-state batteries, *Electrochemical Energy Reviews* **6**, 31 (2023).

[76] A. P. Maltsev, I. V. Chepkasov, and A. R. Oganov, Order-disorder phase transition and ionic conductivity in a $\text{Li}_2\text{B}_{12}\text{H}_{12}$ solid electrolyte, *ACS Applied Materials & Interfaces* **15**, 42511 (2023).

[77] Z. Lu and F. Ciucci, Metal borohydrides as electrolytes for solid-state li, na, mg, and ca batteries: a first-principles study, *Chemistry of Materials* **29**, 9308 (2017).

[78] K. E. Kweon, J. B. Varley, P. Shea, N. Adelstein, P. Mehta, T. W. Heo, T. J. Udovic, V. Stavila, and B. C. Wood, Structural, chemical, and dynamical frustration: origins of superionic conductivity in closo-borate solid electrolytes, *Chemistry of Materials* **29**, 9142 (2017).

[79] B. Wassermann, W. Höhle, and T. Martin, Hexagonal LiI , *Solid state communications* **65**, 561 (1988).

[80] F. W. Poulsen, Ionic conductivity of solid lithium iodide and its monohydrate, *Solid State Ionics* **2**, 53 (1981).

[81] P. Qiu, X. Chen, W. Zhang, G. Zhang, Y. Zhang, Z. Lu, Y. Wu, and X. Chen, A High-Rate and Long-Life Sodium Metal Battery Based on a $\text{NaB}_3\text{H}_8 \cdot x\text{NH}_3@\text{NaB}_3\text{H}_8$ Composite Solid-State Electrolyte, *Angewandte Chemie International Edition* **63**, e202401480 (2024).

[82] X.-W. Chen, J.-X. Kang, Z.-H. Fan, N. Zhang, W.-Y. Zhang, G.-G. Zhang, A.-Q. Zhu, Z.-W. Lu, P. Qiu, Y. Wu, and X. Chen, Sodium octahydridotriborate as a solid electrolyte with excellent stability against sodium-metal anode, *Small* **20**, 2401439 (2024).

[83] J. B. Grinderslev, K. T. Møller, Y. Yan, X.-M. Chen, Y. Li, H.-W. Li, W. Zhou, J. Skibsted, X. Chen, and T. R. Jensen, Potassium octahydridotriborate: diverse polymorphism in a potential hydrogen storage material and potassium ion conductor, *Dalton Trans.* **48**, 8872 (2019).

[84] M. S. Andersson, J. B. Grinderslev, X.-M. Chen, X. Chen, U. Häussermann, W. Zhou, T. R. Jensen, M. Karlsson, and T. J. Udovic, Interplay between the Reorientational Dynamics of the B_3H_8^- Anion and the Structure in KB_3H_8 , *The Journal of Physical Chemistry C* **125**, 3716 (2021).

[85] K. Jun, Y. Chen, G. Wei, X. Yang, and G. Ceder, Diffusion mechanisms of fast lithium-ion conductors, *Nature Reviews Materials* **9**, 887 (2024).

[86] H. Fang and P. Jena, Argyrodite-type advanced lithium conductors and transport mechanisms beyond paddlewheel effect, *Nature Communications* **13**, 2078 (2022).

[87] K. Jun, B. Lee, R. L. Kam, and G. Ceder, The nonexistence of a paddlewheel effect in superionic conductors, *Proceedings of the National Academy of Sciences* **121**, e2316493121 (2024).

[88] Alexandria databases, <https://alexandria.icams.rub.de/>, accessed: 2024-10-04.

[89] J. Schmidt, N. Hoffmann, H.-C. Wang, P. Borlido, P. J. M. A. Carriço, T. F. T. Cerqueira, S. Botti, and M. A. L. Marques, Machine-learning-assisted determination of the global zero-temperature phase diagram of materials, *Advanced Materials* **35**, 2210788 (2023).

[90] H.-L. Yang, B.-W. Zhang, K. Konstantinov, Y.-X. Wang, H.-K. Liu, and S.-X. Dou, Progress and challenges for all-solid-state sodium batteries, *Advanced Energy and Sustainability Research* **2**, 2000057 (2021).

[91] A. Al-Maeeni, M. Lazarev, N. Kazeev, K. S. Novoselov, and A. Ustyuzhanin, Review on automated 2D material design, *2D Materials* **11**, 032002 (2024).

[92] Anonymous, Wyckoff transformer: Generation of symmetric crystals, in *Submitted to The Thirteenth International Conference on Learning Representations* (2024) under review.

[93] F. Pedregosa, G. Varoquaux, A. Gramfort, V. Michel, B. Thirion, O. Grisel, M. Blondel, P. Prettenhofer, R. Weiss, V. Dubourg, J. Vanderplas, A. Passos, D. Cournapeau, M. Brucher, M. Perrot, and E. Duchesnay, Scikit-learn: Machine learning in Python, *Journal of Machine Learning Research* **12**, 2825 (2011).

[94] A. V. Dorogush, V. Ershov, and A. Gulin, Catboost: gradient boosting with categorical features support, arXiv:1810.11363 (2018).

Appendices

A. VALIDATION WITH ML-DRIVEN MD

We perform an additional validation procedure for our predictions using MD simulations driven by an ML-IAP, which allows to significantly scale up the number of validated structures, as compared to the AIMD studies. While all our PES descriptors are calculated with the M3GNet model [16], we choose the newer SevenNet model [47], which outperforms M3GNet on the Matbench Discovery benchmark [48]. These MD simulations are carried out on 30 random structures satisfying the minimal selection described in Sec. II B, as well as on the top 100 structures ordered by the Ξ values. Each structure is simulated at two temperature points of 1000 K and 500 K, with step size of 1 fs and total simulation time of 100 ps for each run. Then, the same procedure as for the AIMD studies is used to extract the conductivity values. Figure 5 shows the distributions of the obtained conductivity values. It can be clearly seen from these plots that Ξ -based selection significantly enhances the sample with structures with high conductivity at both simulated temperature points and at room temperature, the latter being assessed by extrapolation. In order to demonstrate the level of agreement between AIMD and SevenNet, we plot the two sets of the extracted MSD slope values against each other in Fig. 6. Finally, we present the structures that SevenNet confirmed to be superionic, excluding those previously reported in [11, 27, 30], in Table II.

B. COMPARISON OF FV DESCRIPTORS WITH AIMD AND EXPERIMENTAL LABELS

Figures 7 and 8 demonstrate scatter plots with relationships between the labels from the KAHLE2020 and LASKOWSKI2023 datasets, respectively, and the connected and disconnected versions of the FV descriptor at the threshold of 0.5 eV.

C. ALTERNATIVE RANKING MODELS

The ranking descriptor Ξ from Eq. (4) was originally constructed through a visual examination of Figs. 3, 7 and 8. In this section, we describe our work to develop an improved ranking model, using a multivariate analysis of all the introduced descriptors (MPE and FV), referred to collectively as the *PES descriptors*. Additionally, we incorporate the descriptors from the `matminer` library [42], following [27], to evaluate the relative performance of the two descriptor sets, as well as their combined utility.

To make this comparison, we train classification models on the KAHLE2020 dataset with $T = 1000$ K labels, as defined in Sec. II B, and evaluate them using the proce-

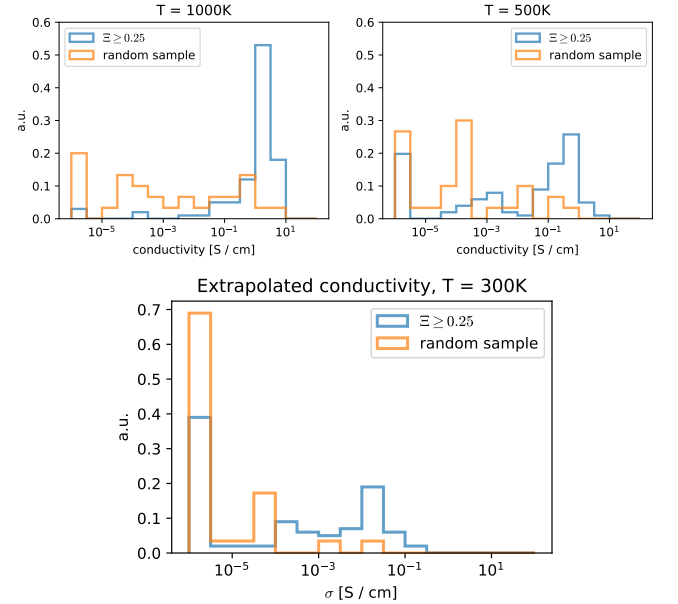


FIG. 5. *Distributions of conductivities estimated with MD driven by SevenNet.* A random sample of size 30 is compared with 100 structures from the top of the Ξ -ordered list. In each panel, both histograms are normalized to have the same total weight. The top left (right) panel shows the distributions of values extracted from the $T = 1000$ K ($T = 500$ K) runs. The bottom panel shows the distributions obtained by extrapolating to the room temperature.

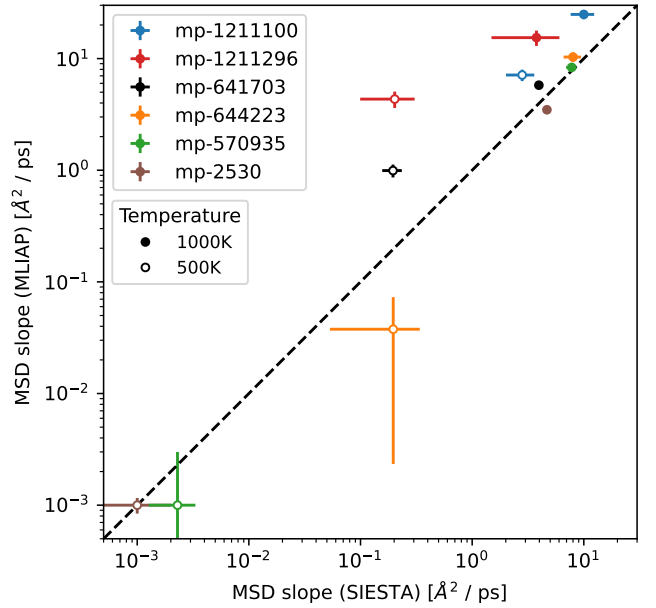


FIG. 6. *MSD slopes comparison between AIMD and SevenNet-driven MD.* All values are clipped from below at $10^{-3} \text{ Å}^2/\text{ps}$. The dashed black line denotes the set of points with $x = y$.

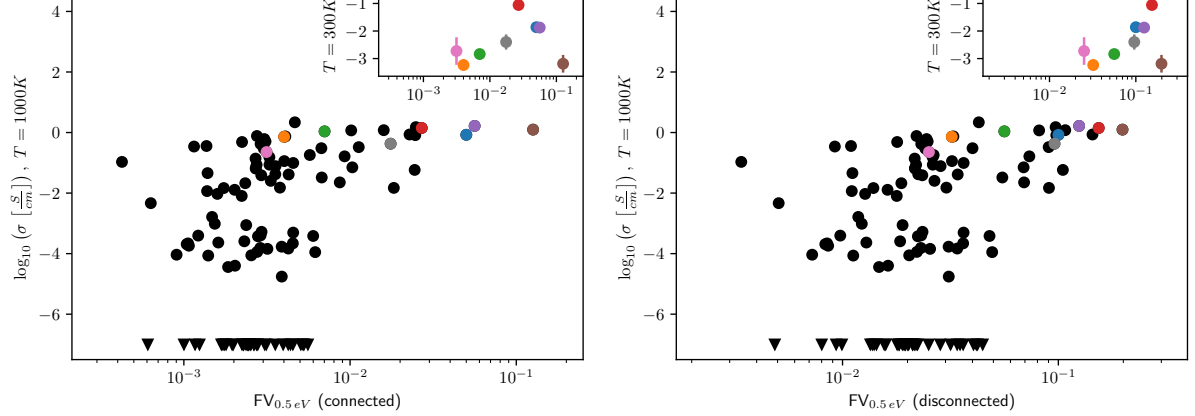


FIG. 7. *Distributions of conductivity labels against FV descriptors for the simulated dataset.* Shown are such distributions for the connected (left) and disconnected (right) versions of the FV descriptors at the threshold of 0.5 eV. The conductivity labels are taken from the 1000 K temperature point in the main plots, while the inset plots show such distributions for the room-temperature-extrapolated conductivity values. As the extrapolated temperature entries are a small subset of the whole dataset, they use per-structure colors in order to relate same structures between the two temperature points. Since the method for extracting the diffusivity constants used in [10] allows for small negative values, such values are clipped at $\sigma = 10^{-7} \text{ S/cm}$ to be kept in the log-scale and shown as triangles in the plots.

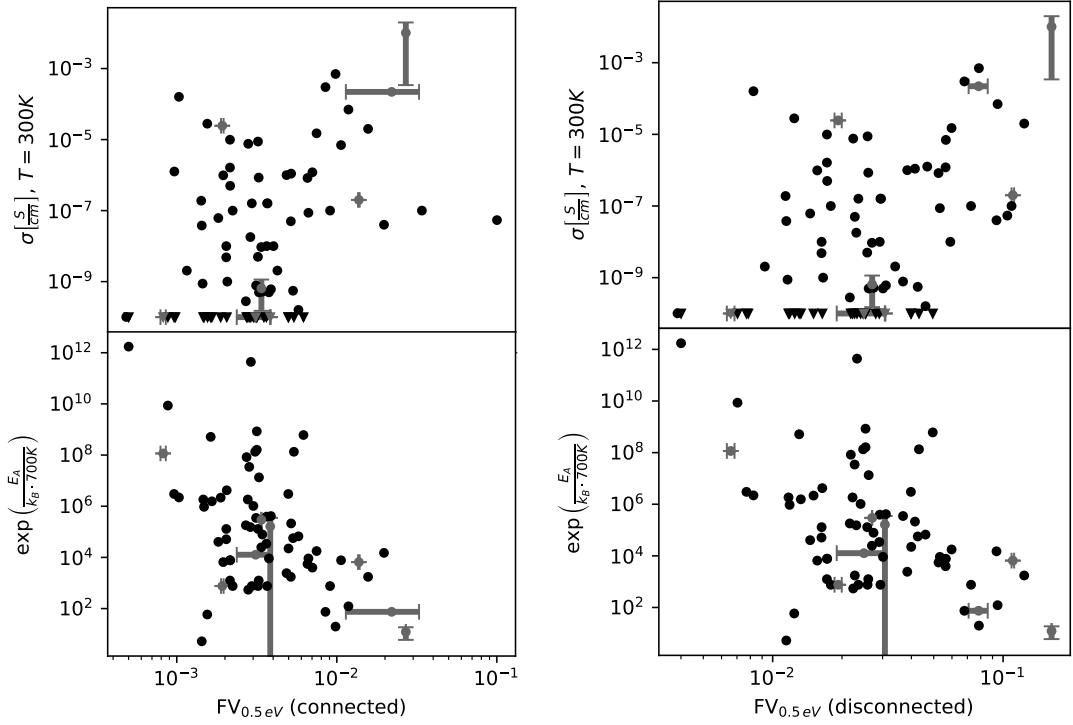


FIG. 8. *Distributions of conductivity and activation energy labels against FV descriptors for the experimental dataset.* Shown are such distributions for the connected (left) and disconnected (right) versions of the FV descriptors at the threshold of 0.5 eV. The top panels show the distributions for the conductivities at room temperature. Extremely low conductivity values are clipped at $\sigma = 10^{-10} \text{ S/cm}$ and are shown as triangles in the plot. The bottom panels demonstrate the activation energies provided in the LASKOWSKI2023 dataset converted to a multiplicative factor relating diffusion constants between $T = 1000 \text{ K}$ and $T = 300 \text{ K}$ via the Arrhenius law. Horizontal error bars are provided for the structures taken from ICSD, where partial occupancy sites are present and a number of concrete structures are sampled. Vertical error bars are shown for the cases where multiple measurements are provided for a single structure.

MP identifier	Composition	System (space group)	Ξ
mp-1211100	LiB ₃ H ₈	Orthorhombic (63)	0.992
mp-1211296	Li(BH) ₆	Cubic (202)	0.99
mp-985583	Li ₃ PS ₄	Orthorhombic (62)	0.958
mp-1001069	Li ₄₈ P ₁₆ S ₆₁	Monoclinic (6)	0.956
mp-1097034	Li ₂₀ Si ₃ P ₃ S ₂₃ Cl	Monoclinic (6)	0.951
mp-1040451	Li ₂₀ Si ₃ P ₃ S ₂₃ Cl	Monoclinic (6)	0.949
mp-1185263	Li ₃ PaO ₃	Cubic (221)	0.942
mp-1097036	Li ₃ PS ₄	Orthorhombic (62)	0.931
mp-1222398	Li ₂ Ga(GeSe ₃) ₂	Monoclinic (9)	0.896
mp-755463	Li ₃ SbS ₃	Trigonal (148)	0.887
mp-753720	Li ₃ BiS ₃	Trigonal (148)	0.858
mp-1222392	LiUI ₆	Monoclinic (5)	0.82
mp-34038	Li ₆ NCl ₃	Monoclinic (8)	0.814
mp-680395	Li ₃ As ₇	Orthorhombic (61)	0.783
mp-775806	Li ₃ SbS ₃	Monoclinic (14)	0.763
mp-28336	Li ₃ P ₇	Orthorhombic (19)	0.721
mp-1222582	Li ₄ GeS ₄	Orthorhombic (33)	0.717
mp-753429	Li ₄ Bi ₂ S ₇	Monoclinic (14)	0.716
mp-985582	Li ₆ PS ₅ I	Cubic (216)	0.703
mp-1177520	Li ₃ SbS ₃	Trigonal (160)	0.658
mp-1211362	Li(BH) ₆	Monoclinic (14)	0.647
mp-1211446	Li ₇ PS ₆	Orthorhombic (33)	0.606
mp-1222482	Li ₆ AsS ₅ I	Triclinic (1)	0.539
mp-1211324	Li ₇ PS ₆	Orthorhombic (33)	0.538
mp-1195718	Li ₄ SnS ₄	Orthorhombic (62)	0.525
mp-950995	Li ₆ PS ₅ I	Monoclinic (9)	0.521
mp-1211176	Li ₆ AsS ₅ I	Monoclinic (9)	0.483

TABLE II. *Top- Ξ candidates confirmed with SevenNet MD that were not predicted in [11, 27, 30].* Reported are the 27 structures (25 after excluding the two containing rare and radioactive elements) from the top-100 highest Ξ list that have extrapolated room temperature conductivity above 1 mS / cm, as predicted with SevenNet MD. Structures already reported in [11, 27, 30] were excluded from this list.

ture outlined in that section. The Leave-One-Out cross-validation technique was employed for model training, where each individual sample is sequentially left out for testing while the remaining samples are used for training. The following three multivariate analysis models were trained: two versions of logistic regression, with L1 and L2 regularization terms, respectively, as implemented in [93], as well as the CatBoost [94] implementation of gradient boosting on decision trees. Each model was separately trained on three feature representations: based on PES descriptors alone, based on **matminer** de-

scriptors alone, as well as on the combination of both. Resulting scores are shown in Fig. 9.

From Fig. 9, it appears that none of the models outperform the Ξ descriptor. Models trained exclusively on the **matminer** descriptors show reasonable scores on the LASKOWSKI2023 experimental dataset, but they sacrifice predictive power on the AIMD data.

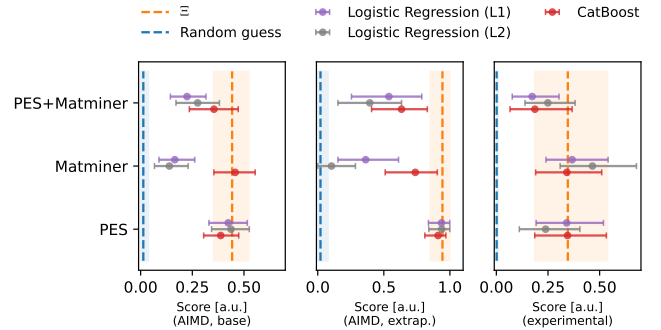


FIG. 9. *Evaluation scores for models trained on the KAHLE2020 dataset using various sets of descriptors.* The scoring procedure is the same as for the results presented in Fig. 3.

D. ALTERNATIVE MSD FITTING WINDOW PARAMETERS

Along with the MSD fitting procedure described in the main text, we consider three alternative options. The first option is to fit the entire MSD trajectory, which doesn't allow to properly estimate the uncertainty of the result but is most sensitive to slowest diffusion processes. The two remaining options are alternative windowed configurations with fitted MSD interval starting from 0 ps and 5 ps, respectively, as opposed to 1 ps chosen in the main procedure. The comparison of the results obtained with the main and the three alternative procedures is shown in Fig. 10. We can clearly see that all four approaches agree in high diffusion regime. In the slow diffusion region, fitting each window from 0 ps overestimates the slopes of MSD due to periodic atomic movement and therefore is inapplicable. Windowed fits with later starting point of 5 ps produce results that are consistent with the 1 ps starting point fits.

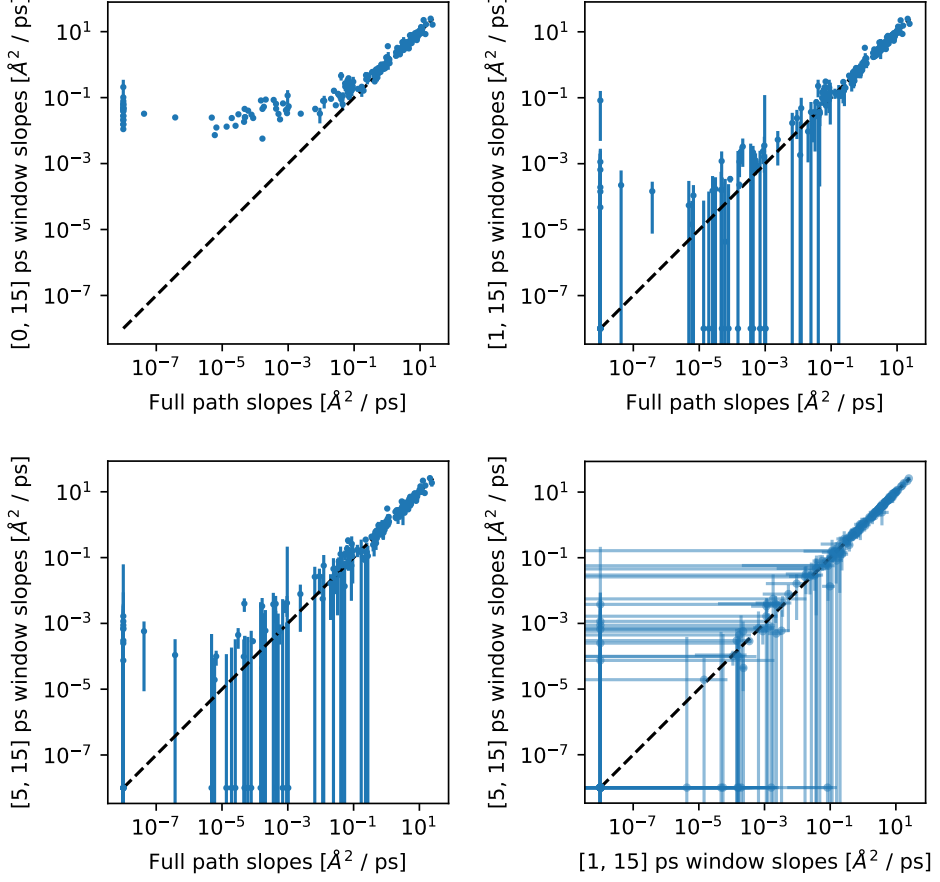


FIG. 10. *MSD slope values extracted with different fitting window parameters.* The results of single fits for the entire simulated trajectory (horizontal axes) are compared with various windowed fit configurations (vertical axes) in top left, top right and bottom left panels, while bottom right panel compares two windowed fit configurations against each other. All windowed fits are performed for 15 ps windows. The starting point of the windowed fits is 0 ps in the top left panel, 1 ps in the top right panel and 5 ps in the bottom left panel. Bottom right panel compares 1 ps and 5 ps fit starting points. The values are extracted from all the SevenNet MD and AIMD runs performed. All values are clipped from below at $10^{-8} \text{\AA}^2 / \text{ps}$. The dashed black line denotes the set of points with $x = y$.